Optical Materials 151 (2024) 115309

Contents lists available at ScienceDirect

Optical Materials

journal homepage: www.elsevier.com/locate/optmat

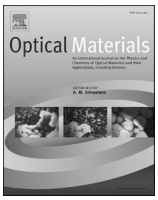

Research Article

Structural, spectroscopi c and laser properties of transparent Tm:$YScO_3$ ceramic based on gas-phase synthesized nanoparticles

R.N. Maksimov [a,b], G. Toci [c], A. Pirri [d,*], V.A. Shitov [a], E. Sani [e], A. Santonocito [f,c], B. Patrizi [c], M. Becucci [g], M. Vannini [c], V.V. Osipov [a]

[a] Institute of Electrophysics UrB RAS, Amundsen St. 106, Ekaterinburg, 620016, Russia
[b] Ural Federal University Named After the First President of Russia B.N. Yeltsin, Mira St. 19, Ekaterinburg, 620002, Russia
[c] C.N.R. – Consiglio Nazionale delle Ricerche, Istituto Nazionale di Ottica, INO, Via Madonna del Piano 10B, I-50019, Sesto Fiorentino, FI, Italy
[d] C.N.R. – Consiglio Nazionale delle Ricerche, Istituto di Fisica Applicata "N. Carrara", IFAC, Via Madonna del Piano 10C, I-50019, Sesto Fiorentino, FI, Italy
[e] C.N.R. – Consiglio Nazionale delle Ricerche, Istituto Nazionale di Ottica, INO, Largo E. Fermi 10, I- 50125, Firenze, FI, Italy
[f] Università degli Studi di Pisa, Dipartimento di Chimica, Via Giuseppe Moruzzi, 13, I-56124, Pisa, Italy
[g] Dipartimento di Chimica "U. Schiff", Università di Firenze, Via della Lastruccia, 3-13, I-50019, Sesto Fiorentino, FI, Italy

ARTICLE INFO

Keywords:
Mixed sesquioxides
Laser ceramics
Gas-phase synthesis
Tm-doped sesquioxides

ABSTRACT

Owing to the combination of good thermo-optical properties and inhomogeneously broadened fluorescence spectra suitable for ultrashort laser pulse generation, rare-earth doped solid solutions of sesquioxides (Y,Lu, Sc)$_2O_3$ have attracted considerable interest in recent years. In this study, compositionally disordered Tm^{3+}-doped $YScO_3$ transparent ceramic was fabricated using solid-state vacuum sintering of nanopowder produced using laser ablation of solid target in air flow. The as-synthesized powder consisted of weakly aggregated spherical particles having 20 nm diameter and a mostly monoclinic (space group *C*2/*m*) crystal structure, whose symmetry was transformed into cubic (space group *Ia*-3) by calcination at 1050 °C. From high resolution transmission electron microscopy (HRTEM) and energy dispersive X-ray analysis (EDX), we observed a homogeneous distribution of components both throughout individual nanoparticles and 100-nm-thick ceramic foil resulting in high structural and optical quality of the obtained samples. The sintered ceramic featured an optical transmission of 77% at 600 nm and above 81% near 2 μm, an average grain size of 24.2 μm and a content of scattering centers of 26.1 ppm. The absorption spectra at several temperatures, from 93 K to 293 K, were measured and the corresponding absorption coefficients were obtained by Lambert-Beer formula in the range from 600 nm to 900 nm and from 1400 nm to 2100 nm. In particular, the room temperature absorption cross section at 794 nm and 1634 nm were determined to be $\sigma_{abs} = 4.25 \times 10^{-21}$ cm^2 and $\sigma_{abs} = 5.01 \times 10^{-21}$ cm^2 respectively. Concerning the emission cross section it was calculated by Fuchtbauer-Ladenburg equation starting from the fluorescence spectrum acquired at the laser work temperature: at 1951 nm and 2106 nm corresponding to the main two emission peaks belonging the curve, it was found $\sigma_{em} = 9.2 \times 10^{-21}$ cm^2 and $\sigma_{em} = 4.9 \times 10^{-21}$ cm^2, respectively. Finally, it was tested the laser behavior of the ceramic: pumped at 793 nm in *quasi*-CW mode it delivered 1.27 W of output power with a slope efficiency of 10.33% at 2081 nm. The tunability curve spans from 1942 nm to 2110 nm (*i.e.* 168 nm).

1. Introduction

Recently, research focusing on the development of ultrafast and broadly tunable solid-state lasers operating in the 2-μm spectral region has gained considerable attention owing to their versatile applications ranging from material processing, environmental monitoring and laser surgery to the generation of mid-infrared supercontinuum and gravitational wave detection [1–7]. The trivalent thulium ion, Tm^{3+}, is a promising candidate to achieve 2-μm laser emission through the $^3F_4 \rightarrow {}^3H_6$ optical transition, thanks to its strong and relatively broad absorption band near 0.8 μm suitable for direct pumping by commercially available high-power AlGaAs based diodes. Despite the relatively high quantum defect, a highly efficient operation of Tm^{3+}-lasers with a slope efficiency well above the Stokes limit can be obtained owing to the so

* Corresponding author.
E-mail address: a.pirri@ifac.cnr.it (A. Pirri).

https://doi.org/10.1016/j.optmat.2024.115309
Received 15 January 2024; Received in revised form 28 March 2024; Accepted 29 March 2024
Available online 9 April 2024

called "*two-for-one*" cross relaxation process ($^3H_4 + {}^3H_6 \rightarrow 2 \times {}^3F_4$), which results in two excited ions for each absorbed pump photon [8].

Among the host materials used for Tm^{3+}-doping, sesquioxides R_2O_3 (R═Y, Lu or Sc) offer several specific advantages in comparison to other material classes such as garnets and fluorides. *This is attributed to their higher thermal conductivity with respect to $Y_3Al_5O_{12}$ in both undoped and doped states for Y_2O_3 and Lu_2O_3* [9]. When compared to fluorides, sesquioxides exhibit improved mechanical characteristics and a superior thermal shock parameter that are essential for power scaling [9,10]. In addition, intentional mixing of different sesquioxides to form a substitutional solid solution $(Y,Lu,Sc)_2O_3$ is an effective strategy for tailoring the laser wavelengths as well as broadening the absorption and emission spectra of Tm^{3+} ions due to a disordered lattice structure [11]. Taken together, these properties significantly elevate the potential of mixed sesquioxides as competitive gain media for ultra-short pulse and tunable lasers.

Considering the properties in mixed matrices, it becomes evident that spectral broadening is more pronounced when an equal contribution is maintained from each host-forming cation in the solid solution. However, the most significant alteration in crystal field strength is expected to occur through combining Y_2O_3 and Sc_2O_3 to form a composition close to $(Y_{0.5}Sc_{0.5})_2O_3$ (from here on called $YScO_3$) because of their larger discrepancies in ionic radii and lattice constants as compared to other pairs, namely $YLuO_3$ and $LuScO_3$ [12–15]. On the one hand, $YScO_3$ fibers and bulk crystals with a cubic bixbyite-type structure have been previously successfully synthesized using various melt growth techniques, including Laser-Heated Pedestal Growth [16,17], the Vertical Gradient Freezing method [18], the Czochralski method [19], and the Floating Zone method [20]. According to the refined Sc_2O_3–Y_2O_3 phase diagram [21], the liquidus temperatures for compositions close to $YScO_3$ are about 400 °C lower than melting points of parent sesquioxides [22], thereby opening the possibility for the Czochralski growth of crystals with relatively good quality using conventional iridium crucibles. On the other hand, despite these findings, only a limited volume fraction of the grown boule is suitable for use as a laser medium. This limitation arises from the potential presence of sub-grains, cracks, and strong internal stresses induced by thermal gradients, along with growth instabilities.

Fabrication of transparent ceramics *via* compaction and sintering of ultrafine powders presents a promising alternative to crystal growth, because the sample size is primarily limited by the furnace chamber dimensions. In addition to reduced synthesis temperature, ceramic technology allows for the preparation of composite gain elements with gradient doping, end cap or absorption edge cladding, which can be extremely challenging or practically impossible to produce in a single-crystalline form [23,24]. It should be noted that most processing methods for manufacturing lasing quality mixed sesquioxide ceramics with Tm^{3+}-doping involve expensive post-treatment with hot isostatic press (HIP) due to the insufficient sinterability of the powders used [25–27]. Furthermore, to effectively utilize HIP for transparent ceramics, it is often necessary to encapsulate pre-sintered samples with platinum [28], which not only subsequently increases costs but also complicates potential mass production.

Previously, we successfully fabricated two series of ceramic samples based on Yb^{3+}-doped solid solutions with various Y/Sc (or Y/Lu) balances by means of conventional vacuum sintering and demonstrated highly efficient laser operation [29–31]. The crucial processing step in our technique is the gas-phase synthesis of nano-sized particles with complex chemical compositions. The high sintering activity of the obtained nanopowders, along with the ability to uniformly incorporate desired sintering additives during vapor condensation, allows us to achieve full densification without the need for costly HIP treatment. Given the assumptions regarding potential scattering loss mechanisms associated with the use of ZrO_2 as a sintering additive [11,19,21], this study focuses on the examination of the uniformity, structural quality, and phase composition of $Tm:YScO_3$ ceramic at various fabrication stages, from nanopowder synthesis to the final sintered sample. Simultaneously, equal emphasis is placed on the detailed investigation and analysis of the spectroscopic properties and laser performance of this composition.

2. Materials and experimental details

2.1. Gas-phase synthesis of $Tm:YScO_3$ nanopowder

Nanoparticles with the Y/Sc balance close to 1 and directly doped by Tm^{3+} ions were synthesized by laser ablation of solid target in air flow [32]. In order to prepare the solid target, commercial high-purity powders of Tm_2O_3 (Tm/(Tm + Total metal impurities) = 99.998%, Lanhit Company, Russia), Sc_2O_3 (Sc/(Sc + Total metal impurities) = 99.99%, Lanhit Company, Russia) and Y_2O_3 (Y_2O_3/(Y_2O_3+Rare-earth oxides) = 99.999%, Nevatorg Company, Russia) were dry-mixed for 24 h in the proportion $Tm_{0.05}(Y_{0.5}Sc_{0.5})_{1.95}O_3$ using a plastic container with an inclined axis of rotation. A small amount of zirconium dioxide (~5 mol.%) acting as grain growth inhibitor was introduced in the mixture. The obtained mixture was compacted into cylinder having 65 mm diameter and then sintered at 1100 °C for 5.5 h in air to reach a mechanical strength suitable for further laser treatment. Due to radiation exposure from a repetitively pulsed CO_2-laser "LAERT", a laser plume containing vapors from the solid target material was generated in proximity to the target's surface. Upon interaction with the surrounding ambient air, the vapors underwent cooling and condensation resulting in the formation of nanoparticles suspended within the evaporating chamber. A specialized mechanism enabled the rotation and linear movement of the target in a horizontal plane, ensuring that the laser beam scanned the target's surface at a constant linear velocity, thereby promoting uniform material evaporation. After completion of surface evaporation, the target transitioned vertically. A fan circulated air through the chamber directing the nanoparticles towards a cyclone and subsequently an electric filter for collection. The air underwent further purification using a mechanical filter before being reintroduced into the chamber. The main laser parameters during the synthesis of nanopowder were as follows: pulse energy – 0.9 J, pulse duration – 330 μs, pulse repetition rate – 500 Hz, peak power – 7 kW, average power – 450 W. The laser beam was focused into 0.75 mm × 0.9 mm-sized elliptical spot by a KCl lens with a power density of 1.3 MW/cm^2. The linear velocity of laser beam movement was 35 cm/s.

2.2. Preparation of transparent $Tm:YScO_3$ ceramic

The synthesized nanoparticles were annealed for 3 h at 1050 °C in air and then uniaxially pressed in a stainless-steel die at 200 MPa to form a cylindrical-shaped green body of 14 mm diameter. The relative density of pressed compact was 43% with respect to the expected X-ray density of the corresponding fully densified composition. The prepared compact was annealed for 3 h at 800 °C in air to burn out the residues of oleic acid used as a lubricant for uniaxial pressing. After annealing, the compact was sintered at for 20 h at 1780 °C under a residual gas pressure of 10^{-3} Pa. Next, the sintered ceramic sample was subjected to calcination for 2 h at 1400 °C for restoring oxygen stoichiometry and then mirror polished on both sides to a thickness of 1.7 mm.

2.3. Characterization methods

The morphological features and compositional uniformity of the as-synthesized nanoparticles were studied using a JEOL JEM 2100 (JEOL Ltd., Japan) transmission electron microscope and a Tecnai G2 F20 transmission electron microscope (TEM, FEI Company, USA) equipped with an EDAX energy dispersive X-ray spectrometer (EDS). The chemical composition of nanopowder was evaluated using an Optima 2100 DV inductively coupled plasma mass spectrometer (ICP MS, Perkin Elmer, USA). The crystal structure of the as-produced nanoparticles and

sintered ceramic was analyzed by means of X-ray diffraction (XRD) using a D8 Discover diffractometer (Bruker AXS, Germany) equipped with an X-ray tube with a copper anode (CuKα1 λ = 1.5406 Å). The thermal behavior of nanopowder was investigated using thermogravimetry and differential thermal analysis (STA 449 F5, NETZSCH, Germany). The internal structure was observed at fractured surface of the samples using a Helios NanoLab 660 scanning electron microscope (SEM, FEI Company, USA). Scanning transmission electron microscopy (STEM) experiments were conducted on thin ceramic foil prepared by the focused ion beam technique in order to investigate the homogeneity of the components' distribution near and at grain-boundaries. Optical microscopy was used to estimate the average volume of pores throughout the depth of the sample by means of the direct counting method [33].

The thermal conductivity of the obtained ceramic was calculated using the following equation: $\kappa = \alpha C_p \rho$, where α is the thermal diffusivity, C_p is the specific heat and ρ is the density. The thermal diffusivity and specific heat were both measured within the temperature interval of 25–300 °C by the laser flash method using an LFA 467 HyperFlash system (NETZSCH, Germany).

The transmission and absorption spectra of the polished sample were measured over the wavelength range from UV to NIR using a Lambda 900 UV–VIS–NIR dual-beam spectrophotometer (PerkinElmer, USA). The sample was mounted on the cold finger of a liquid N_2 cryostat (Specac Variable Temperature Cell), which allows setting the sample temperature in the range from 93 K to 293 K with 0.1 K accuracy. At room temperature (RT) the spectral resolution of the measurements was 1.4 nm (600–900 nm band) and 1.5 nm (1500 nm band); below RT the spectral resolution was 0.6 nm (600–900 nm band) and 0.8 nm (1500 nm band). In order to calculate the emission cross-sections by using the Fuchtbauer-Ladenburg method, the fluorescence spectrum was acquired at RT. The sample was excited at 793 nm and the emerging luminescence was collected at 90° with respect to the excitation direction to avoid the pump beam. The reabsorption effects were minimized by exciting the samples close to the lateral surface.

The micro-Raman measurements were performed using a micro-Raman spectrometer RM2000 (Renishaw, Wotton-under-Edge, UK), which is equipped with a 50x/0.80NA Olympus microscope objective and an Ar excitation-source emitting at 514 nm. The spatial accuracy was higher than 1 μm. The spectral calibration of the spectrometer was checked on the 520 cm^{-1} first order Raman band of bulk silicon; the spectral resolution was 7 cm^{-1} as verified from linewidth measurements on the same silicon calibration band [34]. These measurements were used to analyze the composition uniformity at the sub-grain size scale. In particular, the spectra were acquired in 20 points of the sample along a line (20 μm and 500 μm spacing) and at a depth of about 200 μm below the ceramic's surface. The spatial resolution of the instrument was about 1 μm across and along the line of sight.

2.4. Laser experiments

Fig. 1 shows the laser cavity used to testing the laser behavior of the ceramic. The resonator was formed by three mirrors, namely a plane end mirror (EM), a spherical mirror (SM) and a plane output coupling (OC) mirror with a total length of 170 mm. SM and EM have a high reflectivity in the range of 1.9–2.1 μm and high transmission at the pump wavelength, where OC features a partial reflectivity at the laser wavelength. The uncoated gain element, soldered on a water-cooled copper heat-sink (18 °C) by a thin sheet of indium, has a cylindrical shape with a radius of 5 mm and a thickness of 1.7 mm and is placed in the short arm of the resonator. The distance between EM and the surface of the ceramic was around 2–3 mm. The pump source, a fiber-coupled laser-diode with emission at 793 nm, has an intensity distribution in the focal plane almost cylindrical with a measured beam radius of 50 μm and a numerical aperture of 0.22. The sample was pumped in quasi-CW configuration, with a repetition rate of 10 Hz and a duty factor of 10% for minimizing the thermal effects experienced by the gain material. As the ceramic was uncoated, a special attention was paid to reinject, by a careful alignment of the gain material to the laser cavity, the Fresnel reflections inside the resonator, in order to reduce losses. To maximize the laser performance in free-running, the best coupling was achieved by using three output OCs with different transmissions (T = 1.6, 2.8%, and 9.9%). The tunability of the ceramic laser was tested by placing the OC by a partially reflecting mirror with T = 14.4% and an external grating with 600 lines/mm used in the Littrow's configuration (see Fig. 1b). More details can be found elsewhere [35]. This configuration acts as a coupled cavity scheme, with a master cavity formed by the mirrors EM, SM and OC, and an auxiliary cavity formed by OC and the grating. Briefly, at Littrow's angle the grating acts as an active tuning element as it sends back on the laser mode of the master cavity the first diffraction order. This provides a wavelength selective feedback for lasing while the *zero*-order is used for the output coupling. The laser emission wavelength was recorded by a grating spectrometer equipped with a multichannel optical detector head, with an overall spectral resolution of 0.4 nm.

3. Results and discussion

3.1. Characterization of Tm:$YScO_3$ nanoparticles

It is important to specify the actual Y/Sc balance and Tm^{3+} doping concentration in the particles for proper calculating the absorption and emission characteristics of the fabricated ceramics. From ICP MS analysis, we determined the chemical composition of the as-synthesized

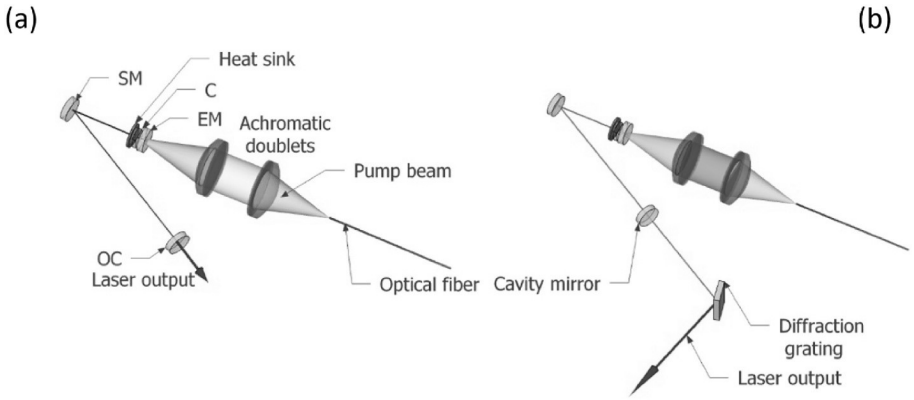

Fig. 1. Non-tunable laser cavity layout (a). C – uncoated ceramic; SM – spherical folding mirror (ROC 100 mm); EM – flat end mirror; OC – flat output coupler mirror. Tunable laser cavity (b): the cavity is closed by a diffraction grating at Littrow's angle.

nanoparticles and the laser target as $(Tm_{0.048}Y_{0.463}Sc_{0.489})_2O_3$ and $(Tm_{0.050}Y_{0.506}Sc_{0.444})_2O_3$, respectively. The composition of nanoparticles obtained by the laser ablation method can sometimes be different from the composition of the initial laser target due to several reasons. In case of mixture of rare-earth sesquioxides the main reason is related to the various thermodynamic properties of the individual components present in the target. Since each sesquioxide has different vaporization and condensation behavior, a slight compositional variation in the nanoparticles compared to the initial target is observed. In addition, this variation can be influenced by laser parameters and surrounding gas environment used during the synthesis of nanoparticles.

For sake of clarity, from here on the composition of nanopowder will be called Tm:$YScO_3$. According to conventional TEM observations (Fig. 2), the powder sample under investigation crystallized in the form of loosely bound aggregates composing of nano-sized particles having a nearly spherical shape and a size range from 6 to 70 nm, while their average size reached 19 nm. From the BET analysis, we determined the specific surface area of the obtained nanopowder and the mass mean diameter as 28.1 m^2/g and 44 nm, respectively. The small size contributes to a larger surface area-to-volume ratio resulting in increased surface forces such as van der Waals forces. However, the presence of surface charges, either from ionization during ablation or adsorbed molecules, creates electrostatic repulsion between the particles preventing close contact and their strong agglomeration. These features are desirable for the fabrication of transparent ceramics as they help to minimize density variations in pressed compacts leading to more uniform densification and improved optical properties.

Fig. 3 shows the scanning transmission electron microscopy (STEM) image and the elemental maps of Tm:$YScO_3$ nanoparticles. All the elements are homogeneously allocated in the sampled individual particles and no core-shell or segregated distribution is observed. The inherent characteristics of laser ablation (such as rapid vaporization, cooling, and condensation) generally favor the synthesis of particles with uniform distribution at the nanoscale level. This promotes the formation of a single-phase solid-solution and helps prevent the segregation of matrix cations and sintering additives leading to consistent and predictable phase composition as well as refractive index throughout the final sintered ceramics. These factors collectively contribute to the material's optical and laser performances. It is important to note that specific experimental conditions and parameters including composition of laser target, laser energy and type of buffer gas allow better controlling the properties of the synthesized nanoparticles.

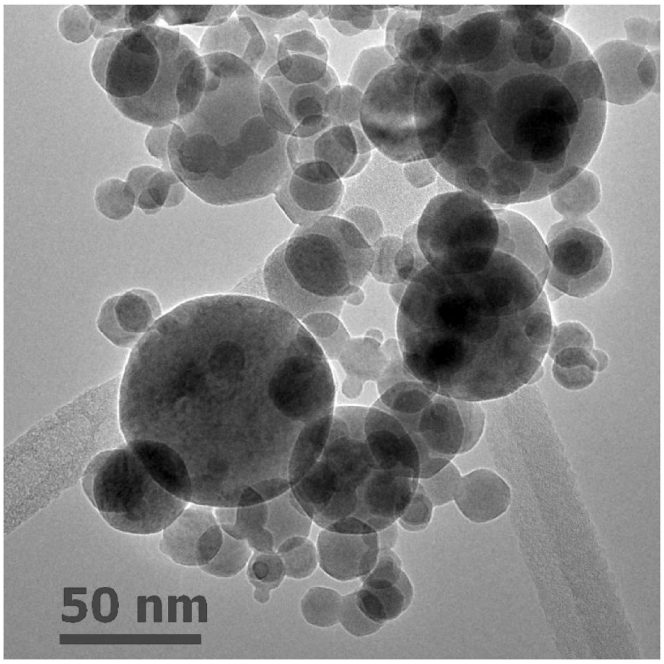

Fig. 2. TEM image showing the morphology of Tm^{3+}:$YScO_3$ nanopowder produced by gas-phase synthesis.

The crystal structure of the as-synthesized Tm:$YScO_3$ nanoparticles was determined by analyzing powder X-ray diffractogram (Fig. 4a). Besides the impact of peak broadening caused by the small crystal size of approximately 19 nm, which is in line with TEM observations, it is evident that the particles do not have the equilibrium structure (space group *Ia*-3, No. 206). The XRD analysis revealed the presence of a mixture of two crystalline phases corresponding to the monoclinic B-type modification of Y_2O_3 (90 wt%, ICDD PDF No. 00-044-0399, see Fig. 4b) and the cubic bixbyite C-type Sc_2O_3 (10 wt%, ICDD PDF No. 00-005-0629, see Fig. 4c). The lattice parameters determined by the crystal structure refinement using the Rietveld method were as follows: a = 13.413 Å, b = 3.446 Å, c = 8.983 Å, β = 98.96° and a = 9.893 Å for the monoclinic and cubic phases, respectively.

The monoclinic phase observed in the obtained Tm:$YScO_3$ nanoparticles can be attributed to a combination of factors such as high-pressure conditions during the laser ablation process and the development of additional strains in the crystal structure. The gas-phase synthesis of Y_2O_3–Sc_2O_3 solid solution can result in its crystallization in a metastable state, a phenomenon attributed to the Gibbs-Thomson effect [36]. In fact, the pressure difference Δp across the curved surface of a spherical particle with a radius r is related to the surface tension γ according to the equation $\Delta p = 2\gamma/r$. Assuming a particle radius of 9.5 nm and a surface tension of 0.74 N/m near the melting point [37], the calculated Δp is approximately 0.156 GPa. The surface tension value can be elevated in nanoparticles compared to a flat surface, leading to an additional increase in pressure.

In previous studies utilizing high-pressure powder and single-crystal X-ray diffraction, it was found that Y_2O_3 and Sc_2O_3 undergo phase transformations from their cubic bixbyite-type structures to the monoclinic B-phase at different pressures. Specifically, Y_2O_3 exhibited this transformation at 11.7 GPa, while Sc_2O_3 underwent the transition at pressures ranging from 25 to 28 GPa [38,39]. At elevated temperatures the C→B phase transition in Y_2O_3 was observed at 3 GPa when the material was heated to 900 °C, whereas Sc_2O_3 required more stringent conditions of 13 GPa and 1000 °C for the transformation to occur [40, 41]. The presence of cubic Sc_2O_3 in the obtained material indicates that there were certain conditions during the synthesis of nanoparticles that favored the formation and stabilization of this phase. However, to fully explain this phenomenon and related mechanisms, a more detailed investigation is required.

The TG/DTA method was used to identify the thermal events that occur during the heating process in the as-synthesized Tm:$YScO_3$ nanopowder. Upon calcination in an air atmosphere, the DTA and H_2O ion current curves clearly exhibit broad peaks within the temperature range of 100–300 °C (Fig. 5). These peaks correspond to the loss of adsorbed moisture and water of crystallization. The weight reduction in this temperature interval amounts to 3.5%, which constitutes more than half of the total weight loss observed at 1250 °C. Furthermore, an exothermic process involving the decomposition of organic compounds takes place within the temperature range of 310–400 °C, resulting in the release of carbon dioxide. This exothermic process is clearly evident in the CO_2 ion current curve. Additionally, an exothermic process is observed between temperatures of 1030–1140 °C and attributed to a transformation of the particles crystal structure from the monoclinic to the cubic phase.

The significant volume change associated with the phase transformation can introduce unwanted internal stresses throughout the powder compact affecting the densification behavior. The presence of internal stresses hinders the movement and rearrangement of particles during sintering and leads to the development of defects such as cracks or voids acting as scattering centers inside the sintered sample. Therefore, it is suggested to perform the B→C phase transformation prior to

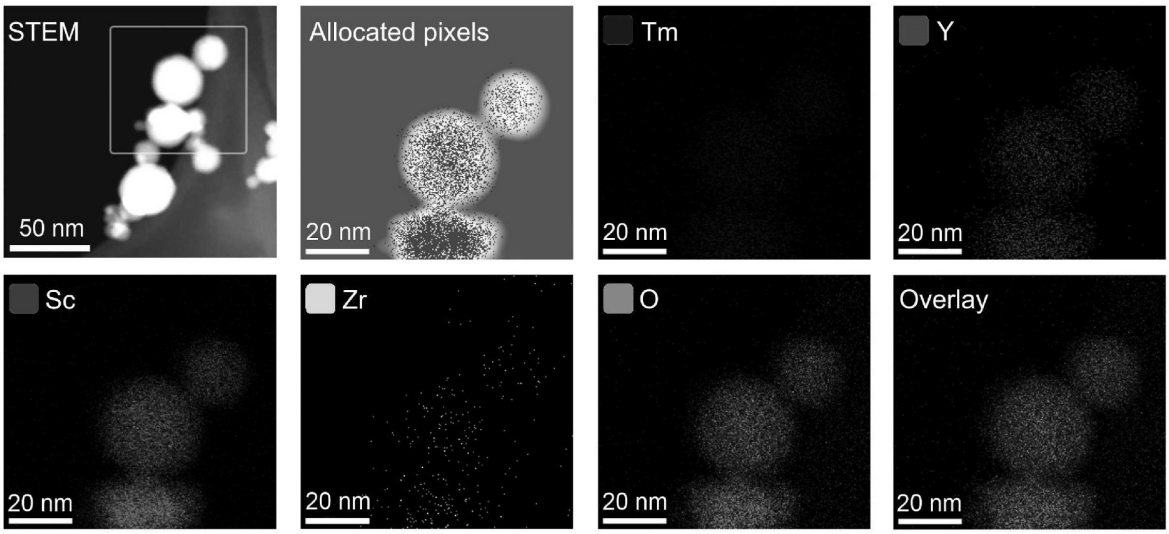

Fig. 3. Dark-field STEM image of the as-synthesized Tm^{3+}:$YScO_3$ nanoparticles and the results of EDX elemental mapping of the probed section.

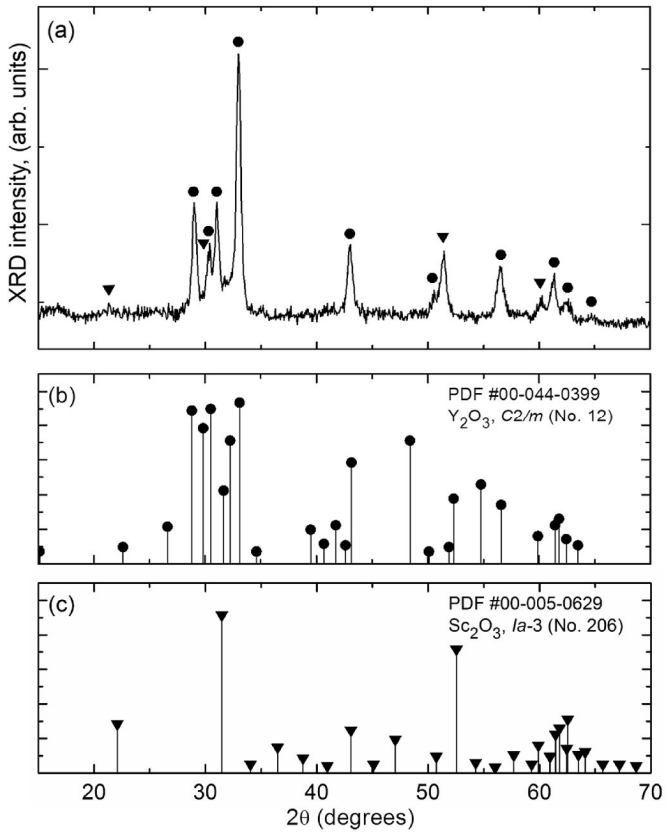

Fig. 4. X-ray diffractogram of Tm^{3+}:$YScO_3$ nanoparticles produced by gas-phase synthesis (a) and reference patterns for monoclinic Y_2O_3 (b) and cubic Sc_2O_3 (c).

compaction of nanopowder by calcination for 3 h at 1050 °C in air. Additional XRD analysis (not shown here) confirmed that the nanoparticles were fully transformed into the stable cubic phase by this heat treatment.

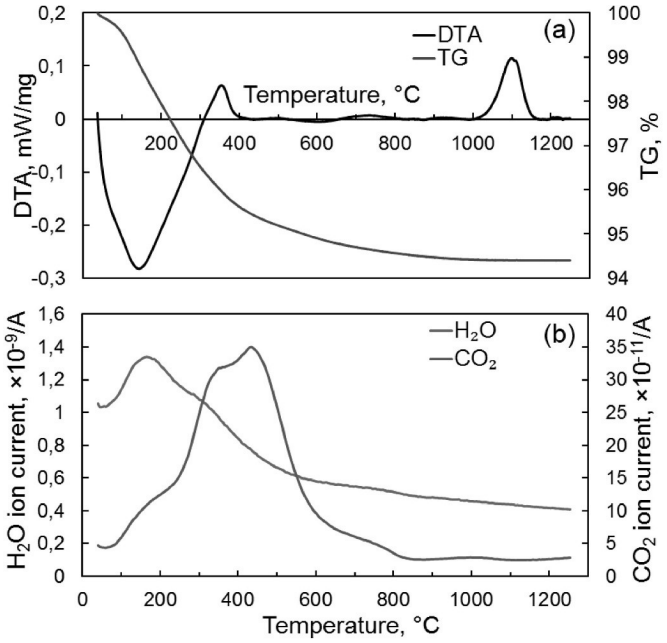

Fig. 5. TG/DTA curves showing the thermal behavior of Tm^{3+}:$YScO_3$ nanopowder (a); CO_2 and H_2O ion current curves (b).

3.2. Structural and thermal properties of the fabricated Tm:$YScO_3$ ceramic

Fig. 6a displays the XRD pattern of the fabricated Tm:$YScO_3$ ceramic. The observed diffraction peaks can be attributed to a single-phase material having a cubic bixbyite structure. The diffraction pattern falls between the theoretical reflections of cubic Y_2O_3 (ICDD PDF No. 00-044-0399, Fig. 6b) and Sc_2O_3 (ICDD PDF No. 00-005-0629, Fig. 6c) indicating formation of substitutional solid solution of sesquioxides. No additional crystalline phases related to the presence of ZrO_2 as a sintering additive were detected. The addition of Sc_2O_3 causes a shifting of peaks towards larger diffraction angles determining the compression of a unit cell. This is expected since the ionic radius of Sc^{3+} (0.745 Å) for VI-fold oxygen coordination is much smaller than that of Y^{3+} (0.900 Å) [12]. The lattice parameter of the ceramic was evaluated to be 10.216 ± 0,005 Å, which is in good agreement with the predicted value of 10.219

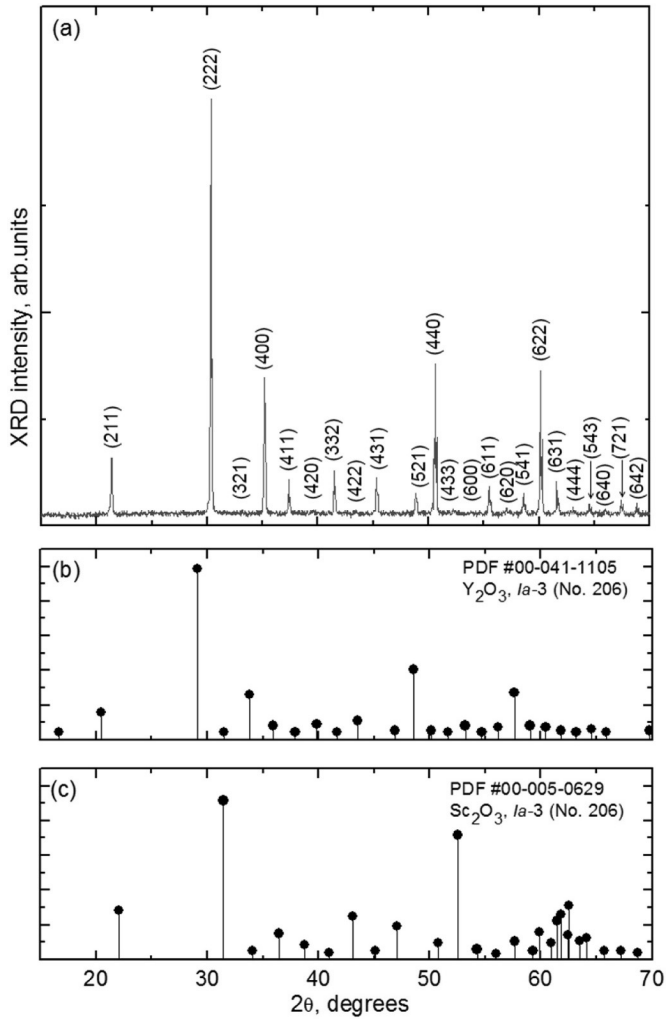

Fig. 6. XRD pattern of the obtained Tm^{3+}:$YScO_3$ ceramic (a) and theoretical XRD patterns of cubic Y_2O_3 (b) and Sc_2O_3 (c).

Å according to Vegard's law.

According to the phase diagrams of the Y_2O_3–Sc_2O_3 and Y_2O_3–Sc_2O_3–ZrO_2 systems previously reported by Schneider et al. and Maister et al. [42,43], a C-type substitutional solid solution was observed near 1900 °C for $(Y_xSc_{1-x})_2O_3$ with x~0.5. It is worth mentioning that under specific experimental conditions, an orthorhombic perovskite yttrium scandate phase with the space group *Pnma* can also be formed. In the corresponding mixture of sesquioxides, a partial transformation into the orthorhombic $YScO_3$ phase occurred after calcination at 1650 °C under ambient pressure for 9.5 h [42], and a pure perovskite modification could be obtained by firing in air at 1000 °C under 20 kbar for 1 h [44]. Additionally, pure perovskite $YScO_3$ was successfully synthesized using specific methods such as heterophase interaction, co-precipitation from hydroxides, and the polymerized complex method [45,46]. However, it should be pointed out that this compound is unstable and transforms into a C-type Y_2O_3–Sc_2O_3 solid solution at temperatures above 1750 °C [42]. Despite the monoclinic structure of the as-obtained nanoparticles used in this study, the Tm:$YScO_3$ nanopowder calcined for 3 h at 1050 °C in air and the ceramic sample vacuum sintered for 20 h at 1780 °C exhibit a single-phase cubic nature as confirmed by XRD analysis.

Microscopic investigations were conducted to ascertain the nature of possible defects responsible for the reduction of optical quality. The fracture surface morphology of the fabricated Tm:$YScO_3$ ceramic is presented in Fig. 7a. The sintered sample exhibits a microstructure characterized by closely packed micro-crystallites with polyhedral shape and an average size of 24.2 μm, which are separated by narrow grain boundaries. All the grain boundaries observed in the ceramic have clean interfaces, as exemplified by the SEM image shown in Fig. 7b. The absence of secondary phases or contaminants eliminates potential regions that could introduce additional light scattering. Under further magnification, see Fig. 7c, the grain boundary reveals a smooth connection between adjacent grains. The boundary appears as a thin, subtle line without any visible segregation or accumulation of zirconia used as a sintering additive indicating a tight alignment of crystal structures without any discernible defects or impurities.

A STEM-EDX analysis was performed to verify the uniformity of the chemical composition in the ceramic sample providing additional confirmation of the homogeneity of the elements at high resolution. Fig. 7d presents a STEM image of a thin ceramic foil specifically focusing on the grain boundary region. The image includes a marked EDS collection line enabling the acquisition of concentration profiles for the mapped elements. Notably, the concentration profiles reveal no segregation of any components confirming a homogeneous distribution of elements across the grain boundary region. Considering the nearly equal segregation coefficients of all cations within the obtained composition (close to 1), it is expected that Y, Sc, and Tm should be uniformly distributed throughout the ceramic. This uniform distribution is likely to result in a homogeneous material with minimal compositional variations or the emergence of secondary phases at grain boundaries. It is suggested that the introduction of Zr having different ionic radius and valence compared to host-forming cations may lead to the formation of localized regions with different chemical compositions, potentially increasing scattering at grain boundaries [11,19,21]. However, neither secondary phases nor intergranular films at grain boundaries were observed in the sintered sample. Our observations highlight the successful demonstration of a well-controlled gas-phase synthesis of mixed sesquioxide nanoparticles and a straightforward fabrication process, eliminating the need for expensive HIP treatment and enabling uniform composition of ceramic at the nanoscale.

Optical microscopy revealed the presence of spherical pores with diameters ranging from 1 to 2 μm. These scattering centers were evenly distributed throughout the depth of the sample (Fig. 8), with the majority being located at grain boundaries and triple junctions. Additionally, a subset of these pores was observed to be intracrystalline. The average volume of the detected pores throughout the depth of the sample was estimated as 26.1 ppm corresponding to 0.00261% decrease in density. The resolution limit of optical microscopy for detecting pores in transparent ceramics is typically around 0.35 μm, roughly half the wavelength of visible light, so that the features of a smaller size cannot be accurately resolved.

Fig. 9 shows the temperature-dependent thermal conductivity of the fabricated Tm:$YScO_3$ ceramic calculated from the experimentally-determined thermal diffusivities, heat capacities, and density. At RT the thermal conductivity reached 4.3 $W\,m^{-1}K^{-1}$, which is comparable to that of a single crystal with a relatively similar composition $(Er_{0.07}Sc_{0.50}Y_{0.43})_2O_3$ [21]. Due to the closely matched atomic mass and ionic radius of Tm^{3+} and Er^{3+}, it is plausible to anticipate a similar level of disorder and consequential impact on the thermal properties when substituting Y^{3+} cations with either Tm^{3+} or Er^{3+} within the Y_2O_3 host matrix. The presence of Sc^{3+} ions, acting as substitutional defects, introduces additional scattering centers for phonons resulting in a reduction of phonon mean free path and deterioration of thermal properties in comparison with parent Y_2O_3 and Sc_2O_3 compositions. Moreover, the phonon mean free path experiences a 1/T decrease beyond the Debye temperature leading to a corresponding decline in thermal conductivity at elevated temperatures, see Fig. 9.

3.3. Spectroscopic investigation

The transmission spectrum of the prepared Tm:$YScO_3$ ceramic is

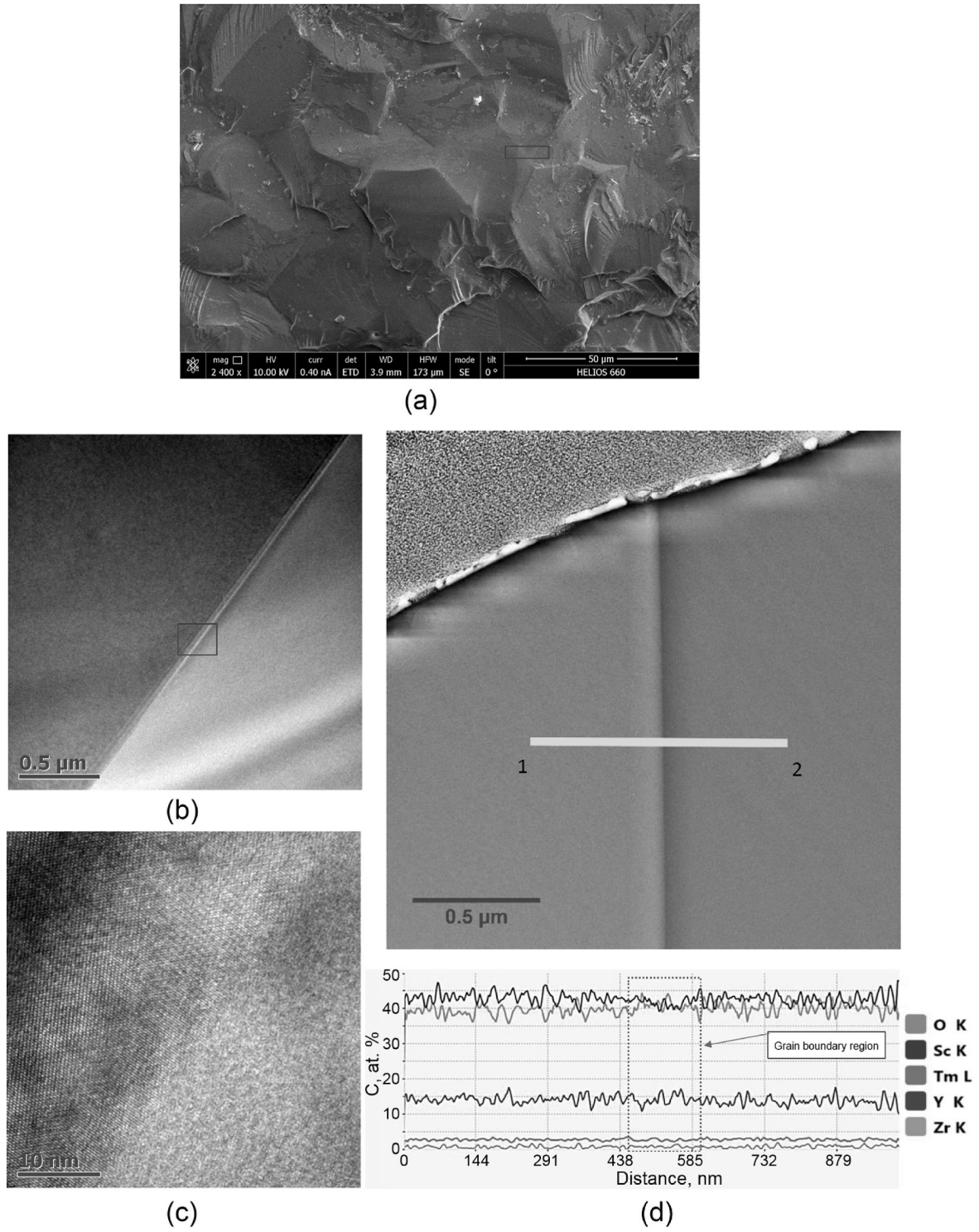

Fig. 7. (a) SEM image showing the microstructure of ceramic sample; the red rectangle marks the extraction area of the foil workpiece; (b) Brightfield image of thin ceramic foil; (c) HRTEM image of the grain boundary obtained from a marked rectangular area; (d) STEM image of thin ceramic foil representing the grain boundary with the marked EDS collection line and concentration profiles of the corresponding mapped elements.

presented in Fig. 10, along with the theoretical transmission curves for Y_2O_3 and Sc_2O_3. These curves were calculated using the refractive index data [47,48] and a modified Fresnel equation that considers multiple light reflections at the interfaces of the sample: $T_0 = 2n/(n^2 + 1)$, where n is the refractive index at the specific wavelength of interest. Apart from the absorption bands of trivalent thulium, the recorded spectrum closely corresponds to the theoretical curves, particularly within the near-infrared segment, while displaying a distinct decline in the visible and UV ranges. Nonetheless, the measured optical transmittances at 600 nm and 1400 nm reached 76.8% and 80.8%, respectively, showing similarity to the transparency levels observed in laser Tm:$YScO_3$ crystals grown by the Czochralski method from iridium crucibles [19]. Considering the systematic comparison of transmittance predictions for Y_2O_3 with a minor volume fraction of monosized spherical pores [49], it

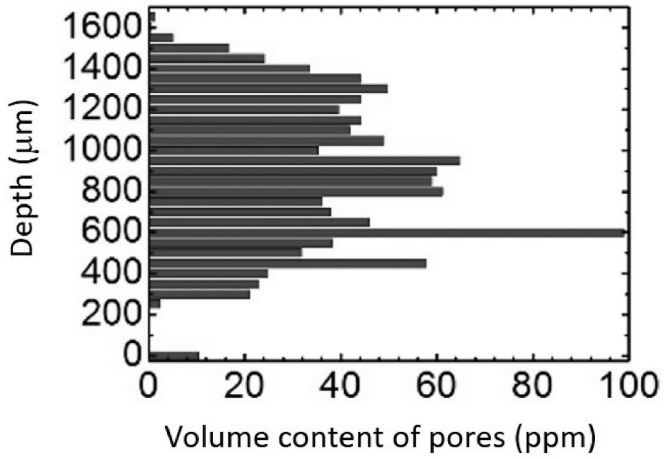

Fig. 8. Distribution of scattering centers throughout the depth of Tm:$YScO_3$ ceramic sample.

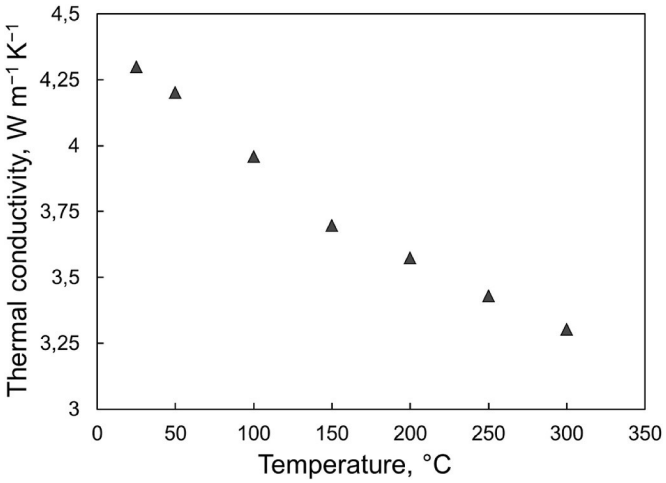

Fig. 9. Temperature dependence of thermal conductivity for the fabricated Tm^{3+}:$YScO_3$ ceramic.

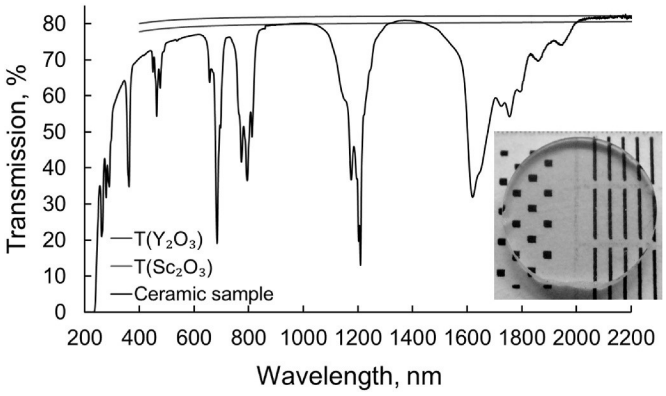

Fig. 10. Photograph and transmission spectrum of the fabricated Tm:$YScO_3$ ceramic along with theoretical transmission curves for undoped parent compositions calculated using refractive index data [47,48].

appears that the transmittances estimated using the van de Hulst approximation align closely with those determined through the exact Mie solutions. Consequently, the presence of residual pores at sub-μm and nm scales in the fabricated sample could significantly contribute to the pronounced reduction in transmission observed at shorter wavelengths. The origin of these pores is linked to various stages of the ceramic's processing, particularly compaction and sintering, rather than being attributed to the presence of ZrO_2.

Micro-Raman spectroscopy was used as a complementary technique to confirm the uniform distribution of components in the sample and highlight an absence of segregation effects among matrix cations. Fig. 11a shows the representative micro-Raman spectrum of the sample. R1, R2 and R3 label on the graph the main Raman modes belonging to the irreducible representation $\mathbf{A_g} + \mathbf{F_g}$ of the space group $Ia\bar{3}$ (point group $2/m\bar{3}$). They were assigned to specific lattice vibration modes by Density Functional Theory (DFT) calculation (carried out with the CP2K software package [50]) with the PBE (Perdew–Burke–Ernzerhof) exchange-correlation functional using the Grimme D3 dispersion correction implemented in CP2K [51,52]. The Goedecker, Teter and Hutter pseudopotentials (GTH) [53] for the Y, Sc, Tm and O atoms were employed with DZVP-MOLOPT-SR-GTH basis set [54] setting a cut-off of 1000 Ry, a Self-Consistent Field convergence threshold equal to 10^{-10} and a convergence criterion for the maximum force component equal to 10^{-5} hartree·$bohr^{-1}$. The algorithm by which the geometric optimization was performed is Broyden–Fletcher–Goldfarb–Shanno algorithm (BFGS) [55], one of the most robust optimizer in CP2K. The analysis of the normal modes of vibration is performed on a simulation cell consisting of 80 atoms in the harmonic approximation and with the Born-Oppenheimer approximation. The potential energy of the system is expanded in Taylor series around the equilibrium geometry in the following way:

$$E_{pot} = E^0_{pot} + \sum_{A}^{n}\left(\frac{\partial E_{pot}}{\partial R_A}\right)\Delta R_A + \frac{1}{2}\sum_{AB}^{n}\left(\frac{\partial^2 E_{pot}}{\partial R_A \partial R_B}\right)\Delta R_A \Delta R_B + \ldots$$

where ΔRα indicates the displacement of the α-*th* position vector (α = A, B, …) from the equilibrium position. Being in the harmonic approximation, the potential is expanded only up to the second term. When the system is in equilibrium geometry, the first derivative is zero by definition, therefore, only the matrix of the second derivatives or force constants is calculated, i.e. the Hessian matrix which is diagonalized to obtain eigenvectors and eigenvalues.

The R1 and R2 vibrational modes are both stretching and bending modes while the R3 vibrational modes are purely stretching modes, the results of the simulations are shown in Table 1, which also shows the comparison with the experimental data.

Due to the presence of Sc^{3+} in the sample, which causes local distortions in the mixed ceramic compared to pure Y_2O_3, there is both a partial removal of degeneracy in highly symmetric modes, along partial superimposition of modes with different symmetries that makes it difficult to clearly distinguish between $\mathbf{A_g}$ and $\mathbf{F_g}$ modes, and leads to the definition of modes with $\mathbf{A_g} + \mathbf{F_g}$ assignment. This is different from pure Y_2O_3, where each Raman-active modes can be assigned a specific irreducible representation (Table 2).

The micro-Raman spectra measured in 20 different points of the sample are shown in Fig. 11(b)–(c). The shape and width as well as the position of the Raman peaks do not change from point to point which is, first, a clear indication of a uniform distribution of the yttrium and scandium ions in the ceramic and, secondly, excludes the coexistence of Y_2O_3 and Sc_2O_3 phases in the investigated volumes.

Fig. 12 reports the absorption coefficients obtained acquiring the absorption spectra at different temperature. All spectra show three main bands placed at 650–710 nm, 750–820 nm and 1.6–1.95 μm due to the Tm^{3+} $^3H_6 \rightarrow {}^3F_{2,3}$, $^3H_4$ and $^3F_4$ transitions. The variation of the absorption coefficients from cryogenic to RT, *i.e.* from 93 K to 253 K, is a clear signature of the dependence of the absorption transitions from the temperature and it can be explained taking into account the change in the thermal population distribution of the sublevels in Tm^{3+} $^3H_6$. When the temperature is varied from 93 K to RT the thermal population in the

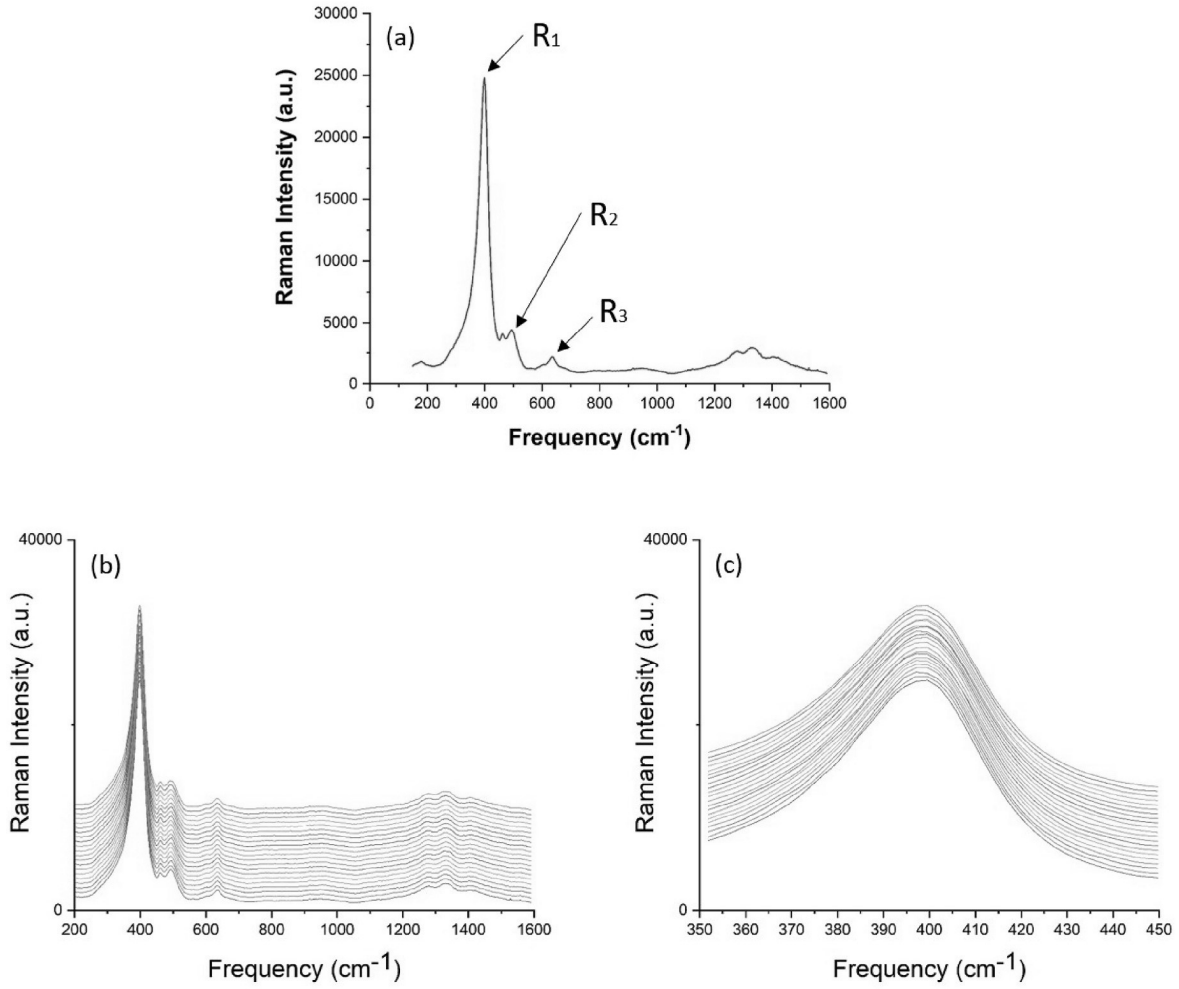

Fig. 11. Micro-Raman spectrum (a); R1=$\mathbf{A_g} + \mathbf{F_g}$, R2=$\mathbf{A_g} + \mathbf{F_g}$ and R3=$\mathbf{A_g} + \mathbf{F_g}$ are label on the graph the main Raman modes. Spectra were acquired in 20 points of each sample along a line. The individual spectra have been translated along the y-axis to facilitate the interpretation of the data by readers.

Table 1
Calculated frequencies of the Raman modes of the sample with their relative irreducible representation, experimental values and percentage relative deviation Δ%. All the frequencies are expressed in cm^{-1}.

Symmetry	our exp.	calc PBE	Δ%
(R_1) $A_g + F_g$	395.11	403.36	2.09%
(R_2) $A_g + F_g$	490.53	499.03	1.73%
(R_3) $A_g + F_g$	634.42	631.58	0.45%

Table 2
Calculated frequencies for the vibrational modes of Y_2O_3 and the irreducible representations for each mode. All the frequencies are expressed in cm^{-1}.

Sym	PBE	Sym	PBE	Sym	PBE
A_g	604.6	**F_g**	589.8 569.7	**E_g**	556.2
	465.3		534.3 473.1		428.0
	378.5		436.5 400.2		326.0
	163.6		382.0 333.7		190.7
			317.6 194.6		
			176.7 168.5		
			123.4 114.1		

upper sublevels increases while that on the lowest sublevel decreases. This redistribution causes an increase of the absorption coefficients linked to the transitions starting from the upper sublevels and a decrease of the transition starting from lower sublevels. According to that, when the temperature is increased, the absorption coefficients decrease in the intervals 650–690 nm, 790–830 nm and 1.6–1.8 μm while increase in 690–710 nm, 800–830 nm and 1.8–2.0 μm. In Table 3 the absorption coefficient values calculated for the main peaks are reported.

Fig. 14 presents the emission cross section spectra, σ_{em}, of the ceramic under investigation and a 5 at.%Tm:Y_2O_3 ceramic fabricated with the same fabrication technique. The spectra were calculated by using the Fuchtbauer-Ladenburg equation. The value of the refractive index was set to 1.8931, which, in turn, was determined by linear interpolation with the Y/Sc content between the values at 2 μm reported in Ref. [56]. The upper level lifetime was set to 3.5 ms for both materials [56]. The two emission bands are centered at 1951 nm and 2106 nm with a FWHM of 58 nm and 54 nm, respectively; the emission cross sections were σem (1951) = 9.2×10^{-21} cm^2 and σ_{em} (2106) = 4.9×10^{-21} cm^2.

3.4. Laser performance

The laser performance of the Tm:$YScO_3$ ceramic exceeds 1.2 W at 2081 nm with a slope efficiency of 10.33% by closing the cavity with the output coupler having T = 1.6%, see Fig. 15.

The tuning range curve is reported in Fig. 16. It is worth to note that its limit on the long wavelengths side is partially determined by the cutoff in the reflectivity of the cavity mirrors. The shortest and longer wavelengths were 1942 nm and 2110, respectively. On the short

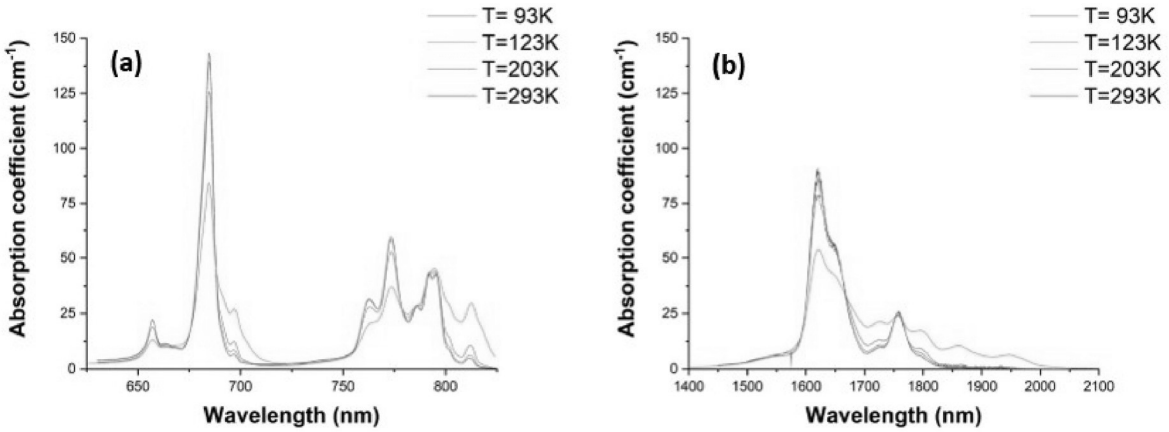

Fig. 12. Absorption coefficients acquired from RT to 93 K in the range from 600 nm to 900 nm (a) and from 1400 nm to 2100 nm (b).

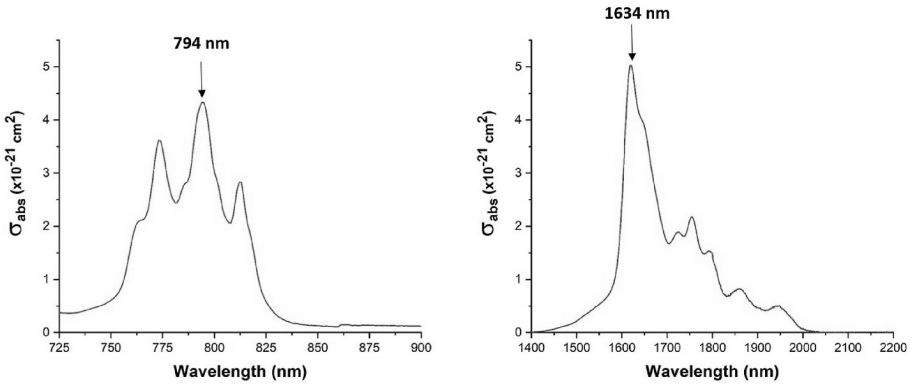

Fig. 13. Absorption cross-sections calculated at RT.

Table 3
Absorption coefficients.

Absorption coefficients (cm^{-1})			
Temperature (K)	93	123	203
Peaks (nm)			
1620.40	90.07	85.49	78.5
1758.80	25.98	25.16	24.00
684.70	143.31	139.44	125.79
773.50	59.52	58.25	52.81

The RT absorption cross section at 794 nm and 1634 nm were $\sigma_{abs} = 4.25 \times 10^{-21}$ cm^2 and $\sigma_{abs} = 5.01 \times 10^{-21}$ cm^2, respectively (see Fig. 13).

wavelength side the tuning is limited by the onset of self-absorption.

As for comparison with other mixed sesquioxides ceramics, Eremeev et al. [57] have reported a maximum output power of about 0.52 W and a maximum slope efficiency of 44% from a $(Tm_{0.050}Y_{0.698}Sc_{0.252})_2O_3$ ceramics, under CW Ti:Sapphire laser pumping. In the present case we obtained about a threefold increase of output power, but with a lower overall slope efficiency. This can be probably attributed to the better mode matching of the pump profile of the Ti:Sapphire laser used in Ref. [57] with respect to the fiber coupled diode laser used in our experiment. Regarding the tuning range, a comparison can be made with the performances obtained from a ceramic sample with composition $(Tm_{0.05}Sc_{0.252}Y_{0.698})_2O_3$, with a similar set up, as reported in Ref. [58]. In the present case the tuning range was slightly less extended on the short wavelength side, but the peak power was slightly higher. Noticeably, in the current case the tuning curve is much smoother and regular across the whole spectrum, with less prevalence of the peak near 2070 nm.

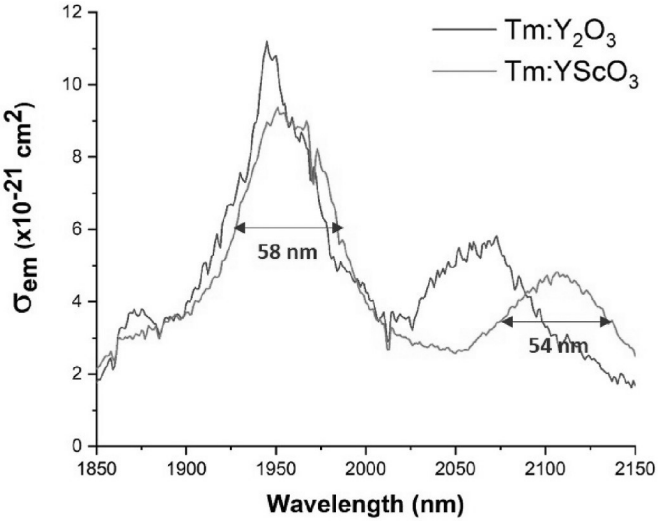

Fig. 14. Emission cross-section spectra calculated at RT. The two main peaks for the Tm:$YScO_3$ ceramic are located at 1951 nm and 2106 nm.

4. Conclusions

In this paper we reported on a 5*at*.%Tm^{3+}:$YScO_3$ mixed transparent ceramic fabricated by solid-state *vacuum sintering* of nanopowders, which were produced using laser ablation of solid target in air flow. We present the fabrication technique, the microstructural and the

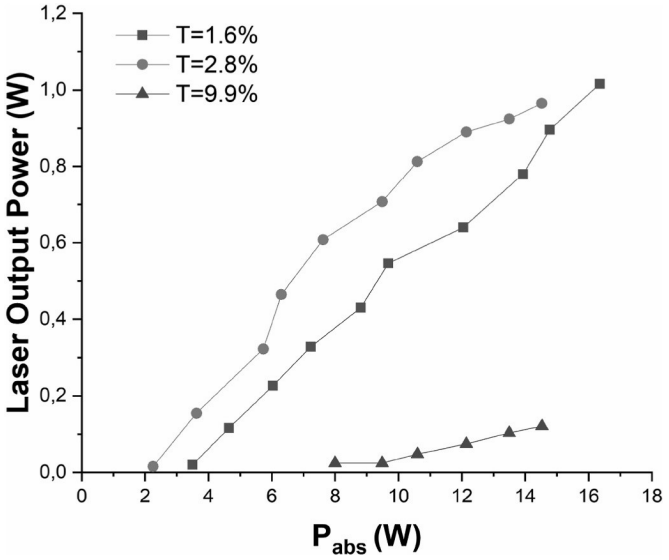

Fig. 15. Laser output power as a function of the absorbed pump power measured by OC mirrors with different transmission. The duty factor was 10%.

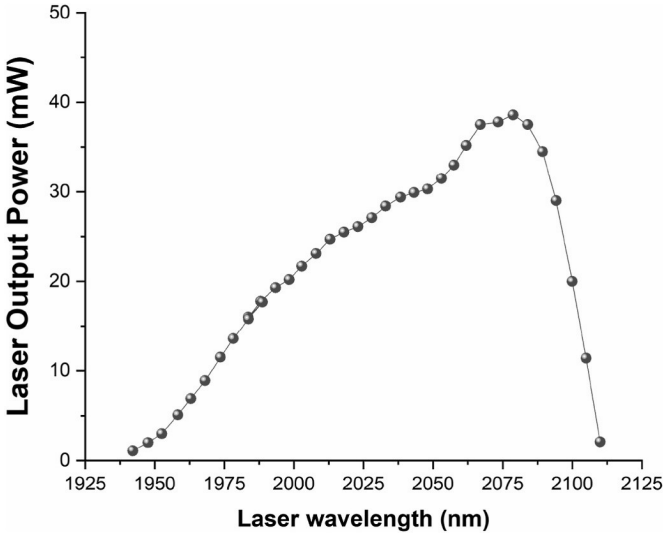

Fig. 16. Tuning curve of Tm^{3+}:$YScO_3$ ceramic laser. The ceramic was pumped in a quasi-CW (10 Hz, DF = 10%).

spectroscopic properties as well as the laser behavior. Moreover, the impact of the mixed composition on the behavior of thulium active ions is investigated.

Microstructural characterization carried out by XRD, HRTEM, EDX and Raman spectroscopy have shown a single-phase nature of the obtained solid solution and a homogeneous distribution of components resulting in high structural and optical quality of the ceramic. No scattering centers related to the zirconium dioxide, used as a sintering additive, were observed near the grain boundary region. The optical transmission of the sample was 77% at 600 nm and above 81% near 2 μm. These results suggest that the gas-phase synthesis of nanoparticles, followed by conventional vacuum sintering, is a promising approach for fabricating mixed sesquioxide transparent ceramics, eliminating the necessity for expensive post-treatments such as hot isostatic pressing.

The absorption spectra acquired from 93 K to 293 K show a strong dependence of the emission peaks on the temperature (T) as by increasing T the typical peaked-structure measured at low temperature is lost with a decrease of the absorption coefficients (see Table 1).

The comparison between the emission cross sections of the mixed sesquioxides ceramic and the pure Tm^{3+}:Y_2O_3 ceramic enlightens the role played by scandium ions. It is observed a shift of around 46 nm toward longer wavelengths of the Tm^{3+}:$YScO_3$ second emission peak (at 2106 nm) respect to the pure Tm^{3+}:Y_2O_3 matrix peak (at 2060 nm). A noticeable effect is observed in terms of FWHM for Tm emission with an increase of approximately 6 nm from Y_2O_3 host (FWHM = 48 nm) to $YScO_3$ host (FWHM = 54 nm).

Concerning the laser behavior, the performance achieved at 2081 nm are comparable with the data reported in literature [58]. Continuously tuned from 1942 nm to 2110 nm (*i.e.* 168 nm), the ceramic shows a tuning range broader than those obtained with Tm: $(Lu_{2/3}Sc_{1/3})_2O_3$ ceramics [59] but narrower than Tm:$LuYO_3$ ceramics [60] and $(Tm_{0.05}Sc_{0.252}Y_{0.698})_2O_3$ ceramic [58] partially due to cutoff in the reflectivity of the cavity mirrors. This represents a clear indication that Tm-doped mixed sesquioxide ceramics can be used to obtain short pulses at ~2 μm.

In comparison to its single-crystalline counterpart [19], this work demonstrates a significant increase in output power, albeit with a notably lower slope efficiency, which we attribute to the better mode matching of the pump profile of the Ti:Sapphire laser used in Ref. [57].

CRediT authorship contribution statement

R.N. Maksimov: Writing – review & editing, Writing – original draft, Project administration, Methodology, Investigation. **G. Toci:** Writing – review & editing, Investigation, Funding acquisition, Conceptualization. **A. Pirri:** Writing – review & editing, Writing – original draft, Investigation, Formal analysis, Data curation. **V.A. Shitov:** Investigation. **E. Sani:** Investigation. **A. Santonocito:** Investigation. **B. Patrizi:** Investigation. **M. Becucci:** Investigation. **M. Vannini:** Visualization. **V.V. Osipov:** Supervision, Funding acquisition, Conceptualization.

Declaration of competing interest

The authors declare that they have no known competing financial interests or personal relationships that could have appeared to influence the work reported in this paper.

Data availability

Data will be made available on request.

Acknowledgements

This work was supported by the state task of IEP UrB RAS and the CNR project SAC. AD002.020.016. The thermal properties of ceramic were studied using the equipment of the Center for Collective Use of the North-Caucasus Federal University financially supported by the Ministry of Education and Science of Russia, unique project identifier RF - 2296.61321X0029 (agreement No. 075-15-2021-687). R. M. acknowledges the partial research funding from the Ministry of Science and Higher Education of the Russian Federation (Ural Federal University Program of Development within the Priority-2030 Program).

References

[1] B. Voisiat, D. Gaponov, P. Gecys, L. Lavoute, M. Silva, A. Hideur, N. Ducros, G. Raciukaitis, Material processing with ultra-short pulse lasers working in 2μm wavelength range, in: Proc. SPIE 9350 (2015), Laser Applications in Microelectronic and Optoelectronic Manufacturing (LAMOM) XX, 2015 935014, https://doi.org/10.1117/12.2078651.

[2] I. Mingareev, F. Weirauch, A. Olowinsky, L. Shah, P. Kadwani, M. Richardson, Welding of polymers using a 2 μm thulium fiber laser, J. Opt. Laser Technol. 44 (2012) 2095–2099, https://doi.org/10.1016/j.optlastec.2012.03.020.

[3] K. Li, C. Niu, C. Wu, Y. Yu, Y. Ma, Development of a 2 μm solid-state laser for lidar in the past decade, Sensors 23 (2023) 7024, https://doi.org/10.3390/s23167024.

[4] U.N. Singh, B.M. Walsh, J. Yu, M. Petros, M.J. Kavaya, T.F. Refaat, N.P. Barnes, Twenty years of Tm:Ho:YLF and LuLiF laser development for global wind and carbon dioxide active remote sensing, Opt. Mater. Express 5 (4) (2015) 827–837, https://doi.org/10.1364/OME.5.000827.

[5] N. Fried, Recent advances in infrared laser lithotripsy, Biomed. Opt Express 9 (9) (2018) 4552–4568, https://doi.org/10.1364/BOE.9.004552.

[6] H. Liu, Y. Yu, W. Song, Q. Jiang, F. Pang, Recent development of flat supercontinuum generation in specialty optical fibers, Opto-Electron. Adv. 2 (2) (2019) 180020, https://doi.org/10.29026/oea.2019.180020.

[7] D.P. Kapasi, J. Eichholz, T. McRae, R.L. Ward, B.J.J. Slagmolen, S. Legge, K. S. Hardman, P.A. Altin, D.E. McClelland, Tunable narrow-linewidth laser at 2 μm wavelength for gravitational wave detector research, Opt Express 28 (3) (2020) 3280–3288, https://doi.org/10.1364/OE.383685.

[8] B. Richards, A. Jha, Y. Tsang, D. Binks, J. Lousteau, F. Fusari, A. Lagatsky, C. Brown, W. Sibbett, Tellurite glass lasers operating close to 2 μm, Laser Phys. Lett. 7 (3) (2010) 177–193, https://doi.org/10.1002/lapl.200910131.

[9] V. Petrov, K. Petermann, U. Griebner, V. Peters, J. Liu, M. Rico, P. Klopp, G. Huber, Continuous-wave and mode-locked lasers based on cubic sesquioxide crystalline hosts, Proc. SPIE 6216 (2006) Laser Source Syst. Technol. Defense Secur. II 12 May 2006 62160H, doi:10.1117/12.665442.

[10] M. Siebold, S. Bock, U. Schramm, B. Xu, J.L. Doualan, P. Camy, R. Moncorge, Yb: CaF_2 – a new old laser crystal, Appl. Phys. B 93 (2009) 327–338, https://doi.org/10.1007/s00340-009-3701-y.

[11] C. Krankel, A. Uvarova, C. Guguschev, S. Kalusniak, L. Hulshoff, H. Tanaka, Detlef Klimm, Rare-earth doped mixed sesquioxides for ultrafast lasers, Opt. Mater. Express 12 (3) (2022) 1074–1091, https://doi.org/10.1364/OME.450203.

[12] R.D. Shannon, Revised effective ionic radii and systematic studies of interatomic distances in halides and chalcogenides, Acta Crystallogr. A A32 (1976) 751–767, https://doi.org/10.1107/S0567739476001551.

[13] F. Hanic, M. Hartmanova, G.G. Knab, A.A. Urusovskaya, K.S. Bagdasarov, Real structure of undoped Y_2O_3 single crystals, Acta Crystallogr. B B40 (1984) 76–82, https://doi.org/10.1107/s0108768184001774.

[14] M. Guzik, J. Pejchal, A. Yoshikawa, A. Ito, T. Goto, M. Siczek, T. Lis, G. Boulon, Structural investigations of Lu_2O_3 as single crystal and polycrystalline transparent ceramic, Cryst. Growth Des. 14 (7) (2014) 3327–3334, https://doi.org/10.1021/cg500225v.

[15] N.D. Todorov, M.V. Abrashev, V. Marinova, M. Kadiyski, L. Dimowa, E. Faulques, Raman spectroscopy and lattice dynamical calculations of Sc_2O_3 single crystals, Phys. Rev. B 87 (2013) 104301, https://doi.org/10.1103/PhysRevB.87.104301.

[16] E. Dobretsova, O. Alimov, D. Guryev, V. Voronov, S. Rusanov, V. Kashin, S. Kutovoy, V. Vlasov, L. Badyanova, I. Novikov, V. Tsvetkov, Structural and spectroscopic features of the bixbyite-type yttrium scandate doped by rare-earth ions, Crystals 12 (12) (2022) 1745, https://doi.org/10.3390/cryst12121745.

[17] O. Alimov, E. Dobretsova, D. Guryev, V. Kashin, G. Kiriukhina, S. Kutovoy, S. Rusanov, S. Simonov, V. Tsvetkov, V. Vlasov, V. Voronov, O. Yakubovich, Growth and characterization of neodymium-doped yttrium scandate crystal fiber with a bixbyite-type crystal structure, Cryst. Growth Des. 20 (7) (2020) 4593–4599, https://doi.org/10.1021/acs.cgd.0c00389.

[18] E. Galenin, V. Galenina, I. Gerasymov, D. Kurtsev, S. Tkachenko, P. Arhipov, S. Sadivnycha, V. Alekseev, A. Shaposhnyk, I. Boiaryntseva, V. Niestierkina, S. Witkiewicz-Lukaszek, Y. Zorenko, O. Sidletskiy, Growth of sesquioxide crystals from tungsten crucibles by vertical gradient freezing method, Crystals 13 (4) (2023) 591, https://doi.org/10.3390/cryst13040591.

[19] A. Suzuki, S. Kalusniak, H. Tanaka, M. Brutzam, S. Ganschow, M. Tokurakawa, C. Krankel, Spectroscopy and 2.1 μm laser operation of Czochralski-grown Tm^{3+}: $YScO_3$ crystals, Opt Express 30 (23) (2022) 42762–42771, https://doi.org/10.1364/OE.475711.

[20] J. Li, W. Hou, Y. Xue, Q. Wang, Q. Song, F. Wang, H. Yu, J. Liu X. Xu, J. Xu, H. Tang, A new near-infrared broadband laser crystal: Cr^{3+} doped $YScO_3$, J. Lumin. 257 (2023) 119710, https://doi.org/10.1016/j.jlumin.2023.119710.

[21] C. Krankel, A. Uvarova, E. Haurat, L. Hulshoff, M. Brutzam, C. Guguschev, S. Kalusniak, D. Klimm, Czochralski growth of mixed cubic sesquioxide crystals in the ternary system Lu_2O_3-Sc_2O_3-Y_2O_3, Acta Crystallogr. B: Struct. Sci, Cryst. Eng. Mater. 77 (2021) 550–558, https://doi.org/10.1107/S2052520621005321.

[22] E.E. Shpil'rain, D.N. Kagan, L.S. Barkhatov, V.V. Koroleva, Measurement of the enthalpy of solid and liquid phases of yttria, HTHP 8 (2) (1976) 183–186. https://www.osti.gov/etdeweb/biblio/7515199.

[23] A. Ikesue, Y.L. Aung, T. Kamimura, S. Honda, Y. Iwamoto, Composite laser ceramics by advanced bonding technology, Materials 11 (2) (2018) 271, https://doi.org/10.3390/ma11020271.

[24] F. Tian, A. Ikesue, J. Li, Progress and perspectives on composite laser ceramics: a review, J. Eur. Ceram. Soc. 42 (5) (2022) 1833–1851, https://doi.org/10.1016/j.jeurceramsoc.2021.12.061.

[25] W. Jing, P. Loiko, J.M. Serres, Y. Wang, E. Vilejshikova, M. Aguiló, F. Díaz, U. Griebner, H. Huang, V. Petrov, X. Mateos, Synthesis, spectroscopy, and efficient laser operation of "mixed" sesquioxide Tm:$(Lu,Sc)_2O_3$ transparent ceramics, Opt. Mater. Express 7 (11) (2017) 4192–4202, https://doi.org/10.1364/OME.7.004192.

[26] H. Wu, G.-H. Pan, Z. Hao, L. Zhang, X. Zhang, L. Zhang, H. Zhao, J. Zhang, Laser-quality Tm:$(Lu_{0.8}Sc_{0.2})_2O_3$ mixed sesquioxide ceramics shaped by gelcasting of well-dispersed nanopowders, J. Am. Ceram. Soc. 102 (2019) 4919–4928, https://doi.org/10.1111/jace.16325.

[27] K. Eremeev, P. Loiko, A. Braud, P. Camy, J. Zhang, X. Xu, Y. Zhao, P. Liu, S. Balabanov, E. Dunina, A. Kornienko, L. Fomicheva, X. Mateos, U. Griebner, V. Petrov, L. Wang, W. Chen, Spectroscopy of solid-solution transparent sesquioxide laser ceramic Tm:$LuYO_3$, Opt. Mater. Express (9) (2022) 3749–3762, https://doi.org/10.1364/OME.471492.

[28] A. Ikesue, Y.L. Aung, V. Lupei, Ceramic Lasers, Cambridge University Press, Cambridge, 2013, p. 455.

[29] A. Pirri, G. Toci, B. Patrizi, R.N. Maksimov, V.V. Osipov, V.A. Shitov, A. S. Yurovskikh, E.V. Tikhonov, M. Becucci, M. Vannini, Yb^{3+}:$(Lu_xY_{1-x})_2O_3$ mixed sesquioxide ceramics for laser applications. Part I: fabrication, microstructure and spectroscopy, J. Alloys Compd. 869 (2021) 159227, https://doi.org/10.1016/j.jallcom.2021.159227.

[30] G. Toci, A. Pirri, B. Patrizi, R.N. Maksimov, V.V. Osipov, V.A. Shitov, M. Vannini, Yb^{3+}:$(Lu_xY_{1-x})_2O_3$ mixed sesquioxide ceramics for laser applications. Part II: laser performances, J. Alloys Compd. 853 (2021) 156943, https://doi.org/10.1016/j.jallcom.2020.156943.

[31] A. Pirri, B. Patrizi, R.N. Maksimov, V.A. Shitov, V.V. Osipov, M. Vannini, G. Toci, Spectroscopic investigation and laser behaviour of Yb-doped laser ceramics based on mixed crystalline structure $(Sc_xY_{1-x})_2O_3$, Ceram. Int. 47 (20) (2021) 29483–29489, https://doi.org/10.1016/j.ceramint.2021.07.116.

[32] V.V. Osipov, V.V. Platonov, V.V. Lisenkov, A.V. Podkin, E.E. Zakharova, Production of nanopowders of oxides by means of fiber and pulse-periodical CO_2 lasers, Phys. Status Solidi C 10 (6) (2013) 926–932, https://doi.org/10.1002/pssc.201200965.

[33] S.N. Bagayev, V.V. Osipov, S.M. Vatnik, V.A. Shitov, I.A. Vedin, V.V. Platonov, I. Sh. Steinberg, R.N. Maksimov, Ho:YAG transparent ceramics based on nanopowders produced by laser ablation method: fabrication, optical properties, and laser performance, Opt. Mater. 50 (A) (2015) 47–51, https://doi.org/10.1016/j.optmat.2015.03.036.

[34] H. Richter, Z.P. Wang, L. Ley, The one phonon Raman spectrum in microcrystalline silicon, Solid State Commun. 39 (5) (1981) 625–629, https://doi.org/10.1016/0038-1098(81)90337-9.

[35] J.E. Bjorkholm, T.C. Damen, J. Shah, Improved use of gratings in tunable lasers, Opt Commun. 4 (4) (1971) 283–284, https://doi.org/10.1016/0030-4018(71)90150-7.

[36] D.A. Porter, K.E. Easterling, M.Y. Sherif, Phase Transformation in Metals and Alloys, third ed., CRC Press, Boca Raton, 2009, p. 521.

[37] J. Paras, O. Takeda, M. Wu, A. Allanore, The surface tension and density of molten Sc_2O_3, La_2O_3, Y_2O_3, Al_2O_3, and MgO measured via a pendant droplet method, Metall. Mater. Trans. B 53 (2022) 2077–2087, https://doi.org/10.1007/s11663-022-02508-3.

[38] S. Jiang, J. Liu, X.-D. Li, Y.-C. Li, S.-M. He, J.-C. Zhang, High-pressure phase transitions of cubic Y_2O_3 under high pressures by in-situ synchrotron X-ray diffraction, Chin. Phys. Lett. 36 (4) (2019) 046103, https://doi.org/10.1088/0256-307X/36/4/046103.

[39] S.V. Ovsyannikov, E. Bykova, M. Bykov, M.D. Wenz, A.S. Pakhomova, K. Glazyrin, H.-P. Liermann, L. Dubrovinsky, Structural and vibrational properties of single crystals of Scandia, Sc_2O_3 under high pressure, J. Appl. Phys. 118 (2015) 165901, https://doi.org/10.1063/1.4933391.

[40] X. Li, X. Xia, H. Xu, S. Zhong, D. He, High-temperature high pressure synthesis of monoclinic Y_2O_3, Mater. Lett. 239 (2019) 82–85, https://doi.org/10.1016/j.matlet.2018.12.068.

[41] A.F. Reid, A.E. Ringwood, High-pressure scandium oxide and its place in the molar volume relationships of dense structures of and ABX_8 type, J. Geophys. Res. 74 (12) (1969) 3238–4252, https://doi.org/10.1029/JB074i012p03238.

[42] S.J. Schneider, R.S. Roth, J.L. Waring, Solid state reactions involving oxides of trivalent cations, J. Res. Natl. Stand. Thecnol. 65A (1961) 345–374, https://doi.org/10.6028/jres.065A.037.

[43] I.M. Maister, L.M. Lopato, Z.A. Zaitseva, A.V. Shevchenko, Interaction in the ZrO_2–Y_2O_3–Sc_2O_3 system at 1300–1900 °C, Izv. Akad. Nauk. SSSR - Neorganicheskiye Mater. 27 (1991) 2337–2340.

[44] J.B. Clark, P.W. Richter, L. Du Toit, High-pressure synthesis of $YScO_3$, $HoScO_3$, $ErScO_3$, and $TmScO_3$, and a reevaluation of the lattice constants of the rare earth scandates, J. Solid State Chem. 23 (1978) 129–134, https://doi.org/10.1016/0022-4596(78)90058-0.

[45] E.S. Lukin, Modern high-density oxide-based ceramics with a controlled microstructure. Part V. Chemical-resistant high-density yttria-, scandia-, and alumina-based ceramics, Refract. Ind. Ceram. 38 (1997) 87–95, https://doi.org/10.1007/BF02767786.

[46] Y. Shimizu, K. Ueda, Phase formation and UV luminescence of Gd^{3+} doped perovskite-type $YScO_3$, J. Solid State Chem. 242 (2016) 170–174, https://doi.org/10.1016/j.jssc.2016.07.023.

[47] A.A. KaminskiĬ, K. Ueda, A.F. Konstantinova, H. Yagi, T. Yanagitani, A.V. Butashin, V.P. Orekhova, J. Lu, K. Takaichi, T. Uematsu, M. Musha, A. Shirokava, Lasing and refractive indices of nanocrystalline ceramics of cubic yttrium oxide Y_2O_3 doped with Nd^{3+} and Yb^{3+} ions, Crystallogr. Rep. 48 (2003) 1041–1043, https://doi.org/10.1134/1.1627445.

[48] K. Takaichi, H. Yagi, P. Becker, A. Shirakawa, K. Ueda, L. Bohatý, T. Yanagitani, A. A. Kaminskii, New data on investigation of novel laser ceramic on the base of cubic scandium sesquioxide: two-band tunable CW generation of Yb^{3+}:Sc_2O_3 with laser-diode pumping and the dispersion of refractive index in the visible and near-IR of undoped Sc_2O_3, Laser Phys. Lett. 4 (2007) 507–510, https://doi.org/10.1002/lapl.200710020.

[49] S. Hribalova, W. Pabst, Modeling light scattering by spherical pores for calculating the transmittance of transparent ceramics - all you need to know, J. Eur. Ceram. Soc. 41 (4) (2021) 2169–2192, https://doi.org/10.1016/j.jeurceramsoc.2020.11.046.

[50] T.D. Kühne, M. Iannuzzi, M.D. Ben, V.V. Rybkin, P. Seewald, F. Stein, T. Laino, R. Z. Khaliullin, O. Schütt, F. Schiffmann, D. Golze, J. Wilhelm, S. Chulkov, M.

H. Bani-Hashemian, V. Weber, U. Borstnik, M. Taillefumier, A.S. Jakobovits, A. Lazzaro, H. Pabst, T. Müller, R. Schade, M. Guidon, S. Andermatt, N. Holmberg, G.K. Schenter, A. Hehn, A. Bussy, F. Belleflamme, G. Tabacchi, A. Glöß, M. Lass, I. Bethune, C.J. Mundy, C. Plessl, M. Watkins, J. VandeVondele, M. Krack, J. Hutter, CP2K: an electronic structure and molecular dynamics software package-Quickstep: efficient and accurate electronic structure calculations, J. Chem. Phys. 152 (19) (2020), https://doi.org/10.1063/5.0007045.

[51] J.P. Perdew, K. Burke, M. Ernzerhof, Generalized gradient approximation made simple, Phys. Rev. Lett. 77 (1996) 3865, https://doi.org/10.1103/PhysRevLett.77.3865.

[52] S. Grimme, J. Antony, S. Ehrlich, H. Krieg, A consistent and accurate Ab initio parametrization of density functional dispersion correction (DFT-D) for the 94 elements H-Pu, J. Chem. Phys. 132 (2010), https://doi.org/10.1063/1.3382344.

[53] S. Goedecker, M. Teter, J. Hutter, Separable dual-space Gaussian pseudopotentials, Phys. Rev. B 54 (1996) 1703, https://doi.org/10.1103/PhysRevB.54.1703.

[54] J. VandeVondele, J. Hutter, Gaussian basis sets for accurate calculations on molecular systems in gas and condensed phases, J. Chem. Phys. 127 (2007) 114105, https://doi.org/10.1063/1.2770708.

[55] J.D. Head, M.C. Zerner, A Broyden-Fletcher-Goldfarb-Shanno, optimization procedure for molecular geometries, Chem. Phys. Lett. 122 (1985) 264–270, https://doi.org/10.1016/0009-2614(85)80574-1.

[56] C. Krankel, Rare-earth-doped sesquioxides for diode-pumped high-power lasers in the 1-, 2-, and 3-μm spectral range, IEEE J. Sel. Top. Quant. Electron. 21 (1) (2014) 250–262, https://doi.org/10.1109/JSTQE.2014.2346618.

[57] K. Eremeev, P. Loiko, R. Maksimov, V. Shitov, V. Osipov, D. Vakalov, V. Lapin, P. Camy, W. Chen, V. Petrov, A. Braud, Highly efficient lasing and thermal properties of Tm: Y 2 O 3 and Tm:(Y, Sc) 2 O 3 ceramics, Opt. Lett. 48 (15) (2023) 3901–3904, https://doi.org/10.1364/OL.495516.

[58] A. Pirri, R.N. Maksimov, V.A. Shitov, V.V. Osipov, E. Sani, B. Patrizi, M. Vannini, G. Toci, Continuously tuned $(Tm_{0.05}Sc_{0.252}Y_{0.698})_2O_3$ ceramic laser with emission peak at 2076 nm, J. Alloys Compd. 889 (2021) 161585, https://doi.org/10.1016/j.jallcom.2021.161585.

[59] Y. Wang, W. Jing, P. Loiko, Y. Zhao, H. Huang, X. Mateos, S. Suomalainen, A. Härkönen, M. Guina, U. Griebner, V. Petrov, Sub-10 optical-cycle passively mode-locked Tm:$(Lu_{2/3}Sc_{1/3})_2O_3$ ceramic laser at 2 μm, Opt Express 26 (8) (2018) 10299–10304, https://doi.org/10.1364/OE.26.010299.

[60] Y. Zhao, L. Wang, W. Chen, Z. Pan, Y. Wang, P. Liu, X. Xu, Y. Liu, D. Shen, J. Zhang, M. Guina, X. Mateos, P. Loiko, Z. Wang, X. Xu, J. Xu, M. Mero, U. Griebner, V. Petrov, SESAM mode-locked Tm:LuYO3 ceramic laser generating 54-fs pulses at 2048 nm, Appl. Opt. 59 (33) (2020) 10493–10497, https://doi.org/10.1364/AO.408650.